Phase transformation and microstructural development of zirconia/stainless steel bonded with a Ti/Ni/Ti interlayer for the potential application in solid oxide fuel cells

Shen-Hung Wei and Chien-Cheng Lin[a)]
Department of Materials Science and Engineering, National Chiao Tung University, Hsinchu 30050, Taiwan

(Received 12 December 2013; accepted 28 February 2014)

The 8 mol% yttria-stabilized zirconia (8Y-ZrO_2) was bonded to stainless steel 316L at 900 °C for 1 h in a protective Ar atmosphere using an interlayer of Ti/Ni/Ti. Interfacial microstructures were characterized using both secondary electron microscope (SEM) and transmission electron microscope (TEM), each with an attached energy dispersive spectroscope (EDS). A layer sequence of σ-phase/$TiFe_2$/TiFe + β-Ti/Ti_2Fe was observed at the stainless steel 316L/Ti interface, whereas a layer sequence of Ti_2Ni/Ti_2Ni + TiNi/$TiNi_3$ was found at the Ti/Ni interface. Furthermore, TiO and c-ZrO_{2-x} formed at the Ti/8Y-ZrO_2 interface. An acicular α-Ti and a fine ω-phase existed along with β-Ti in the residual Ti foil adjacent to the stainless steel 316L, but α-Ti and Ti_2Ni were observed within β-Ti in the other residual Ti foil adjacent to the 8Y-ZrO_2. The orientation relationships of the ω-phase and β-Ti were $[1\bar{1}0]_{\beta\text{-Ti}}//[1\bar{2}10]_{\omega}$ and $(111)_{\beta\text{-Ti}}//(0001)_{\omega}$, respectively. The microstructural development was elucidated with the aid of Fe–Ti and Ni–Ti binary phase diagrams.

I. INTRODUCTION

Zirconia (ZrO_2) can be partially or fully stabilized by incorporating various contents of yttria (Y_2O_3) or other aliovalent oxides. This incorporation is accompanied with the formation of oxygen vacancies to maintain local electroneutrality. A concentrated oxygen vacancy gives rise to high oxygen-ion mobility in the stabilized ZrO_2 because of the rapid diffusion of oxygen ions by the vacancy mechanism. The fast oxygen ionic conduction with negligible electronic conductivity makes doped-ZrO_2 one of the most useful electroceramics for many applications.[1] Previous studies reported that the highest ionic conductivity is obtained with 8 mol% Y_2O_3-stabilized ZrO_2, hereafter named 8Y-ZrO_2.[2,3]

The 8Y-ZrO_2 is an electrolyte with adequate ionic conduction and stability at high temperatures. These attributes make this composition the primary electrolyte used by most SOFC developers and researchers. An SOFC is regarded as a primary electrochemical device for converting the chemical energy in fuels into electrical energy because of its high thermal efficiencies, fuel flexibility, low levels of pollution, and low cost compared with other energy conversion devices. The typical SOFC configuration uses a porous Ni/YSZ cermet as the anode and a porous lanthanum-strontium-manganite (LSM) as the cathode. Planar SOFCs are formed by combining the anode-electrolyte-cathode structure with the stainless steel interconnect that provides an electrical connection.[4,5] However, it is difficult to obtain a hermetic joint between 8Y-ZrO_2 and the stainless steel connection because of mismatches in the coefficients of thermal expansion (CTE), volume changes (related to phase transformation), poor wetting (related to surface energy differences), and so forth.

A large mismatch in the CTEs leads to residual stress in the ceramic-metal joint after cooling from the working temperature,[6] which eventually reduces the strength and reliability of the joints and even creates cracks along the ceramic/metal interface. In general, ferritic steels are used as interconnects for SOFCs operating at a high temperature (800 °C) because they have similar CTEs to that of 8Y-ZrO_2.

Despite high CTEs, austenitic steels have high room temperature ductility, creep resistance, and oxidation resistance and a reduced interaction of the interconnect with cathode and anode; therefore, they are potential interconnect materials for SOFCs operating at a relatively low temperature (600 °C). Molin et al. evaluated the potential application of porous stainless steel 316L as a SOFC stack.[7] Niewolak et al. investigated the potential suitability of ferritic and austenitic steels as interconnect materials for SOFCs operating at 600 °C.[8]

The development of a method for fabricating stainless steel/8Y-ZrO_2 joints that can withstand the SOFC operating temperatures is of great interest. In the last decade, various methods have been developed to make stainless steel/8Y-ZrO_2 joints.[6,9–11] The methods involving

[a)]Address all correspondence to this author.
e-mail: chienlin@faculty.nctu.edu.tw
DOI: 10.1557/jmr.2014.65

liquid-phase formation, such as brazing[11] and partial transient liquid-phase bonding (PTLPB),[12–15] have received the most attention. In brazing, active elements (Ti, Zr, Hf, etc.) are added to the braze filler to enhance the wettability and form a stable chemical bond. Active brazing with the Ag–Cu–Ti brazing alloy is frequently used to join ceramics and is considered the most effective method.[16] However, the active elements in the filler increase the brittleness of the joints. These joints most likely remelt below the original bonding temperatures and soften at even lower temperatures, limiting their use in structural applications. In addition, brazing with noble-based metals, such as Au or Ag, significantly increases manufacturing costs.

Solid-state diffusion bonding can also be an effective technique to join metals and ceramics, if suitable interlacing foils are chosen. In this study, a set of Ti/Ni/Ti multilayers, not a commercial interlayer alloy, was used for joining 8Y-ZrO_2 and stainless steel 316L below the eutectic temperatures of Ni–Ti and Fe–Ti. Two Ti foils were used as active media to form a chemical bond, whereas the Ni foil, a soft metal, acted as a buffer layer to relieve residual thermal stresses from the large CTE mismatch between ceramic and metal.

Previous studies primarily focused on observing the new phases formed at the interface using secondary electron microscopy (SEM) with a resolution of the micron and submicron scales. In this study, various interfacial microstructures were characterized using the transmission electron microscope with an attached energy dispersion spectrometer (TEM/EDS). An attempt was made to explore the formation mechanism of individual reaction layers, as well as their microstructural development, with the aid of binary phase diagrams.

II. EXPERIMENTAL PROCEDURE

Hot-pressed 8Y-ZrO_2 bulks (2 mm thick, CTE: 10.5 × 10^{-6}/K (25–1000 °C), Chenbros Metal Co. Ltd., Kaohsiung, Taiwan) and stainless steel 316L sheets (5 mm thick, CTE: 16.5–19.5 × 10^{-6}/K (25–1000 °C), Henan Billions Chemicals Co. Ltd., Calgary, Canada) simulated the electrolyte and the interconnect of an SOFC, respectively. The Ni foil (100 μm thick, CTE: 13.3–16.3 × 10^{-6}/K (25–900 °C), 99.5 wt.% pure, annealed, Alfa Aesar, Ward Hill, MA) and the Ti foil (50 μm thick, CTE: 8.9–10.1 × 10^{-6}/K (25–1000 °C), 99.6 wt.% pure, annealed, Alfa Aesar, Ward Hill, MA) were used as the core and outer layers, respectively. The specifications of these starting materials are listed in Table I. Stainless steel 316L and 8Y-ZrO_2 specimens were thermally joined with the Ti/Ni/Ti interlayer at 900 °C for 1 h in a tube furnace (Model STF54434C, Lindberg/Blue, Thermo Elec. Inc., Houston, TX). Figure 1 displays the assembly of the specimen and fixture separated with two graphite foils. The specimen was hand tightened by screw and bolt. Prior to joining, the stainless steel 316L specimens were ground with SiC emery papers, and the 8Y-ZrO_2 specimens were ground with a 15-μm diamond matted disc on a precision polishing machine (Model Minimet 1000, Buehler Ltd., Lake Bluff, IL). Then, the 8Y-ZrO_2 specimens were polished to a 0.5 μm surface finish with a diamond paste using the precision polishing machine mentioned above. All specimens were ultrasonically cleaned in acetone and then air-dried.

TABLE I. Nominal compositions of starting materials.

Materials	Composition (wt.%)
316L SS	<60.9 Fe, 16.00–18.00 Cr, 12.00–15.00 Ni, <2.00–3.00 Mo, <2.00 Mn, <1.00 Si, <0.045 P, <0.03 C, <0.03 S
8Y-ZrO_2	>86.7 ZrO_2 + HfO_2, 13.3 ± 0.4 Y_2O_3, <0.002 TiO_2, <0.02 SiO_2, <0.002 MgO, <0.02 Cl^-, <0.01 Fe_2O_3, <0.01 Na_2O, <0.01 Al_2O_3, <0.002 CaO, <1.0 L.O.I[a]
Ti foil	99.6 wt.% Ti, <0.4 wt.% C, N, Fe
Ni foil	99.5 wt.% Ni, <0.5 wt.% C, N, Fe

[a]L.O.I = loss on ignition.

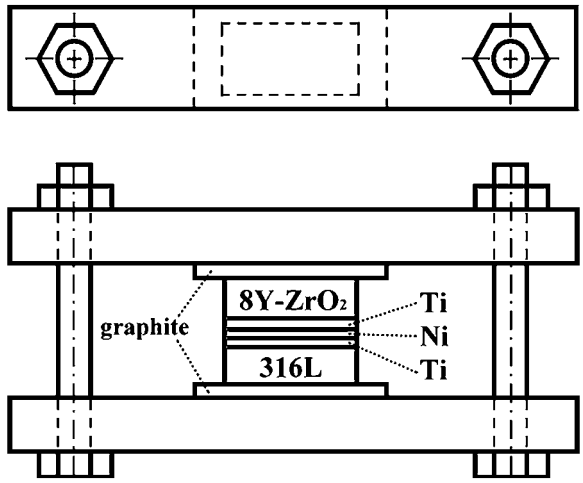

FIG. 1. Experimental assembly.

To prevent the samples from being oxidized, the working chamber was pre-evacuated to 1 × 10^{-4} Pa and purged with Ar for at least four cycles. Thereafter, the tube furnace was refilled with an argon protective atmosphere at a slightly positive pressure. The heating rate and the cooling rate of the joint were 5°C/min and 3°C/min, respectively.

Cross-sectional SEM specimens were cut, ground, and polished using the standard procedures described previously.[11] TEM specimens were prepared using the FIB lift-out technique (FIB, Model Nova 200, FEI Co., Hillsboro, OR).[17] The TEM specimens were less than 100 nm in thickness and were electron transparent. Prior to the FIB milling, a layer of Pt approximately 1 μm thick

was deposited by ion beam chemical deposition using $C_9H_{16}Pt$ as a precursor gas. The Pt layer served as a marker and prevented the outer surface of the sample from being directly exposed to the Ga^+ ion beam implantation during subsequent ion milling operations. The FIB milling was performed with a Ga^+ ion beam at 30 keV. After rough milling (7–1 nA), polishing (0.5–0.1 nA), and final polishing (50–10 pA), a thin foil (17 μm × 2 μm × 0.05 μm) was cut off and transferred to a TEM grid (Formvar/Carbon Coated-Copper 200 mesh) using a micromanipulator for subsequent TEM analyses.

The microstructures of various reaction zones were characterized using a scanning electron microscope (Model JSM 6500F, JEOL Ltd., Tokyo, Japan) and a TEM (Model JEM 2000 FX, JEOL Ltd., Tokyo, Japan), each with an attached energy dispersive spectrometer (Model ISIS 300, Oxford Instrument Inc., London, UK). The Cliff-Lorimer standardless technique[18] was performed for TEM/EDS to analyze the compositions for the various phases. The crystal structures of various phases were obtained from the analyses of selected area diffraction patterns (SADPs) using computer-simulation software of crystallography (CaRIne Crystallography 3.1, Divergent S. A., Compiègne, France).

III. RESULTS AND DISCUSSION

A. SEM/EDS analyses

Figure 2(a) displays the backscattered electron image (BEI) of a cross-section of the stainless steel 316L/8Y-ZrO_2 joint with a Ti/Ni/Ti multilayer filler after annealing at 900 °C for 1 h. Extended reactions occurred at the stainless steel 316L/Ti, Ti/Ni, and Ti/8Y-ZrO_2 interfaces, designated as reaction zones I, II, and III, respectively. Each zone exhibited several further reaction layers, designated as A through G. Figure 2(b) shows the BEI of the stainless steel 316L/Ti interface (zone I), where there were four distinct reaction layers, designated as layers A, B, C, and D, because of the strong chemical affinity of Fe to Ti. Several Fe–Ti intermediate reaction

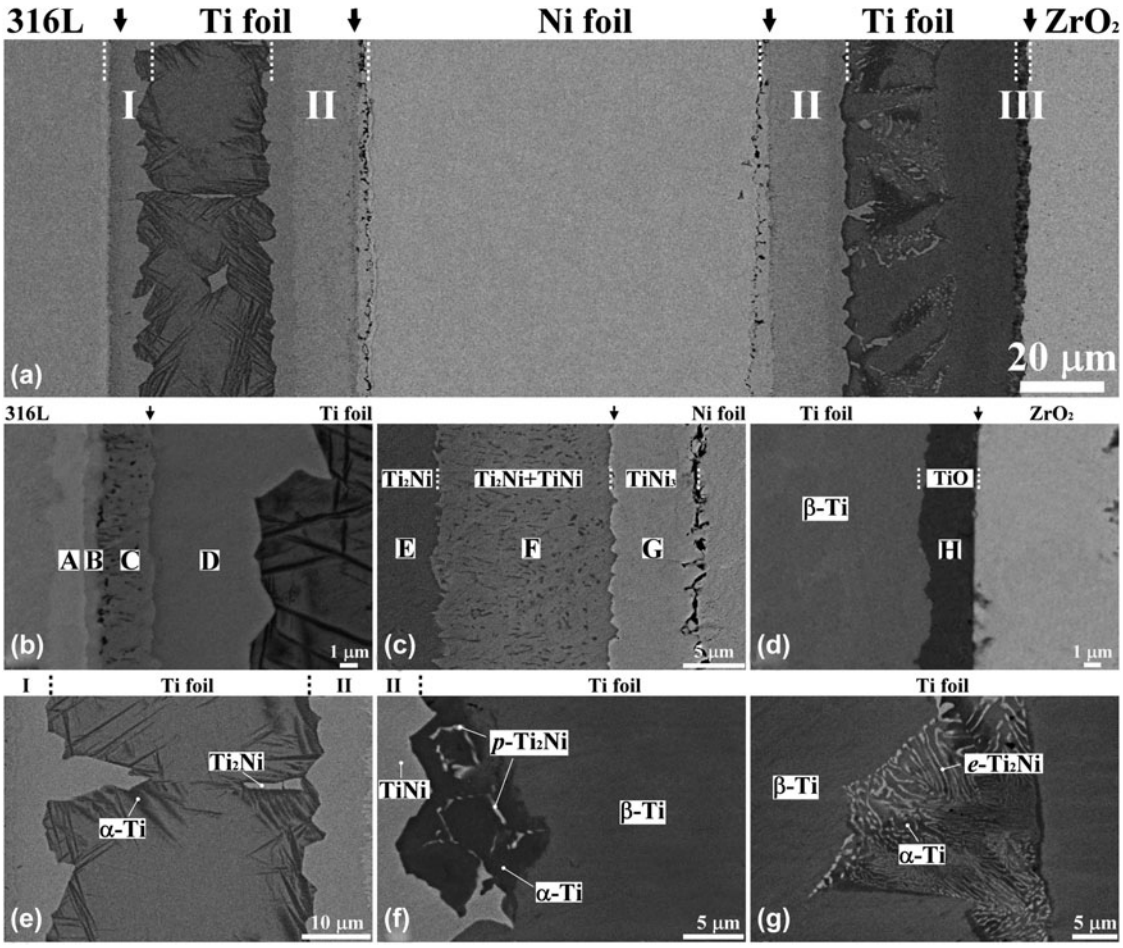

FIG. 2. (a) SEM BEI micrograph of the interfacial layers of the 316L/8Y-ZrO_2 joint with a Ti/Ni/Ti interlayer after annealing at 900 °C for 1 h. In addition, the magnified micrographs of (b) the 316L/Ti interface (zone I), (c) the Ti/Ni interface (zone II), (d) the Ti/8Y-ZrO_2 interface (zone III), (e) the residual Ti between 316L and Ni, (f and g) the residual Ti between Ni and 8Y-ZrO_2 are shown. The vertical arrows in the upper side indicate the original interfaces. *p*-Ti_2Ni and *e*-Ti_2Ni represent proeutectoid Ti_2Ni and eutectoid Ti_2Ni, respectively.

layers formed with a densely dispersed β-Ti phase in layer C. The relative contrast of these layers reflected a decreasing Fe/Ti ratio from the left to right sides because of the atomic number effect of the BEI as shown in Fig. 2(b). Figure 2(c) shows that zone II consisted of three layers, designated as layers E, F, and G, at the Ti/Ni interface. A darker layer (layer E) abutting the Ti foil at the left side consisted of 64.3 at.% Ti and 35.7 at.% Ni, indicating the formation of the Ti_2Ni intermediate phase. A bright thin layer (layer G) adjacent to the Ni foil at the right side was composed of 25.8 at.% Ti and 74.2 at.% Ni, corresponding to the $TiNi_3$ intermetallic compound. A two-phase layer (TiNi + Ti_2Ni) (layer F) was found between reaction layers E and G. The Ti_2Ni formed in layer F most likely precipitated as the second phase in the TiNi matrix during cooling. Extended pores were found at the $TiNi_3$/Ni interface. The Kirkendall effect caused the formation of pores because Ni diffused to the Ti side faster than Ti did to the Ni side.[19] Figure 2(d) displays that zone III was composed of a thin layer, designated as layer H, at the Ti/8Y-ZrO_2 interface. This thin layer contained 44.6 at.% Ti, 54.3 at.% O, and 1.1 at.% Zr, indicating the formation of titanium oxide (TiO).[20]

Residual Ti and Ni foils were also observed because of their limited reactions at the interfaces of 316L/Ti, Ni/Ti, and Ti/8Y-ZrO_2. The two residual Ti foils, which mainly remained as α-Ti and/or β-Ti, exhibited very different microstructures, whereas the residual Ni foil was a single phase with Ti in solid solution. As shown in Fig. 2(e), the residual Ti foil between zones I and II consisted of the mixed α + β Ti structure and Ti_2Ni islands. Where a large Ti_2Ni grain existed, the neighboring area was depleted of Ni, facilitating the formation of the needle-like α-Ti. The composition of the β-Ti was 94.3 at.% Ti, 3.7 at.% Fe, 1.1 at.% Cr, and 0.9 at.% Ni. The β-Ti retained after cooling from 900 °C existed because it was stabilized by the dissolution of Fe, Cr, and Ni.[21] Figures 2(f) and 2(g) show that the residual Ti foil between zones II and III contained three phases, including β-Ti (gray), Ti_2Ni (bright), and α-Ti (dark). The retained β-Ti consisted of 88.6 at.% Ti, 10.9 at.% Ni, and 0.5 at.% O. As shown in Fig. 2(f), *p*-Ti_2Ni nucleated and grew at the α-Ti grain boundaries. Figure 2(g) also shows a eutectoid colony with the (α-Ti and *e*-Ti_2Ni) lamellar structure from the hypereutectoid reactions. Here, *p*-Ti_2Ni and *e*-Ti_2Ni represented pro-eutectoid Ti_2Ni and eutectoid Ti_2Ni, respectively.

IV. TEM/EDS ANALYSES

A. Microstructure of the stainless steel 316L/Ti interface

Figure 3(a) reveals a bright-field image (BFI) of reaction zone I with four reaction layers, i.e., reaction layers A, B, C, and D, adjacent to the stainless steel 316L. The corresponding reaction layer sequence is as follows: σ-phase, $TiFe_2$, TiFe + β-Ti, and Ti_2Fe from stainless steel 316L to Ti. As shown in Fig. 3(b), the SADP of reaction layer A indicates that it belonged to the SADP of a tetragonal crystallographic structure along the zone axis of [001] with the calculated lattice parameters a = 0.91 nm and c =0.47 nm. Figure 3(c) shows the energy dispersive spectrum (EDS) of reaction layer A, consisting of 54.8 at.% Fe, 35.2 at.% Cr, 3.4 at.% Ti, 2.9 at.% Ni, 2.6 at.% Mo, and 1.1 at.% Cu. Thus, reaction layer A most likely corresponded to a σ-phase (for comparison, σ-FeCr: a = 0.87995 nm and c = 0.45442 nm in JCPDS #50708) with a homogeneity range from 50 to 57.5 at.% Fe, based on the Fe–Cr binary phase diagram. Previous studies indicated that the σ-phase was also found in both Ti/steel and Ti alloy/steel interfaces.[21–24]

Figure 3(d) shows the SADP of the reaction layer B, corresponding to a hexagonal crystallographic structure ($MgZn_2$ type) with the calculated lattice parameters a = 0.50 and c = 0.85 nm. The EDS, as shown in Fig. 3(e), indicates that the phase in reaction layer B contained 51.7 at.% Fe, 32.3 at.% Ti, 10.9 at.% Cr, 2.1 at.% Mo, 1.5 at.% Ni, and 1.5 at.% Cu. From the Darken-Gurry (D-G) map (electronegativity versus metallic radius), high solubility in a specific solvent is predicted if the solute and solvent are close to each other in the periodic table.[25] The D-G map indicated that the solubility of Cr or Ni in Fe was larger than that of Cr or Ni in Ti.[26] As mentioned above, the phase in reaction layer B corresponded to the $TiFe_2$ phase with Ti:(Fe + Cr + Ni) = 32:64 ≈ 1:2[26] (for comparison, $TiFe_2$: a = 0.4785 nm, c = 0.7799 nm in JCPDS #150336).

Reaction layer C was composed of two phases, TiFe and β-Ti. Figure 3(f) illustrates that the SADP of the TiFe phase along the zone axis of [111] corresponded to a simple cubic CsCl structure with the calculated lattice parameter a = 0.30 nm (for comparison, FeTi: a = 0.2975 nm in JCPDS #190636). Figure 3(g) shows that the TiFe phase in reaction layer C was composed of 51.9 at.% Ti, 36.9 at.% Fe, 4.7 at.% Cr, 3.5 at.% Ni, 1.7 at.% Cu, and 1.3 at.% Mo with Ti:(Fe + Cr + Ni) = 52:45 ≈ 1:1.[26] The other phase (grain size <0.4 μm) found in reaction layer C was identified as β-Ti. The EDS result of the β-Ti in reaction layer C showed that it contained 2.2 at.% Cr, 1.4 at.% Cu, 0.5 at.% Fe, and 0.3 at.% Ni in solid solution. Grot and Spruiell indicated that TiFe decomposed into β-Ti and TiFe during cooling because the composition range of Ti narrowed with decreasing temperature.[27]

Figure 3(h) illustrates that the SADP of the phase found in reaction layer D represented a complex fcc crystallographic structure with the calculated lattice parameter a = 1.15 nm, which is consistent with the Ti_2Ni type structure. Figure 3(i) shows the EDS result of the phase in reaction layer D, consisting of 65.9 at.% Ti, 19.3 at.% Fe, 11.4 at.% Ni, 2.1 at.% Cu, and 1.3 at.% Cr. The result corresponded to the Ti_2Fe phase with Cr, Ni, and Mo in solutions [Ti:(Fe + Cr + Ni) = 66:31 ≈ 2:1].[26] In

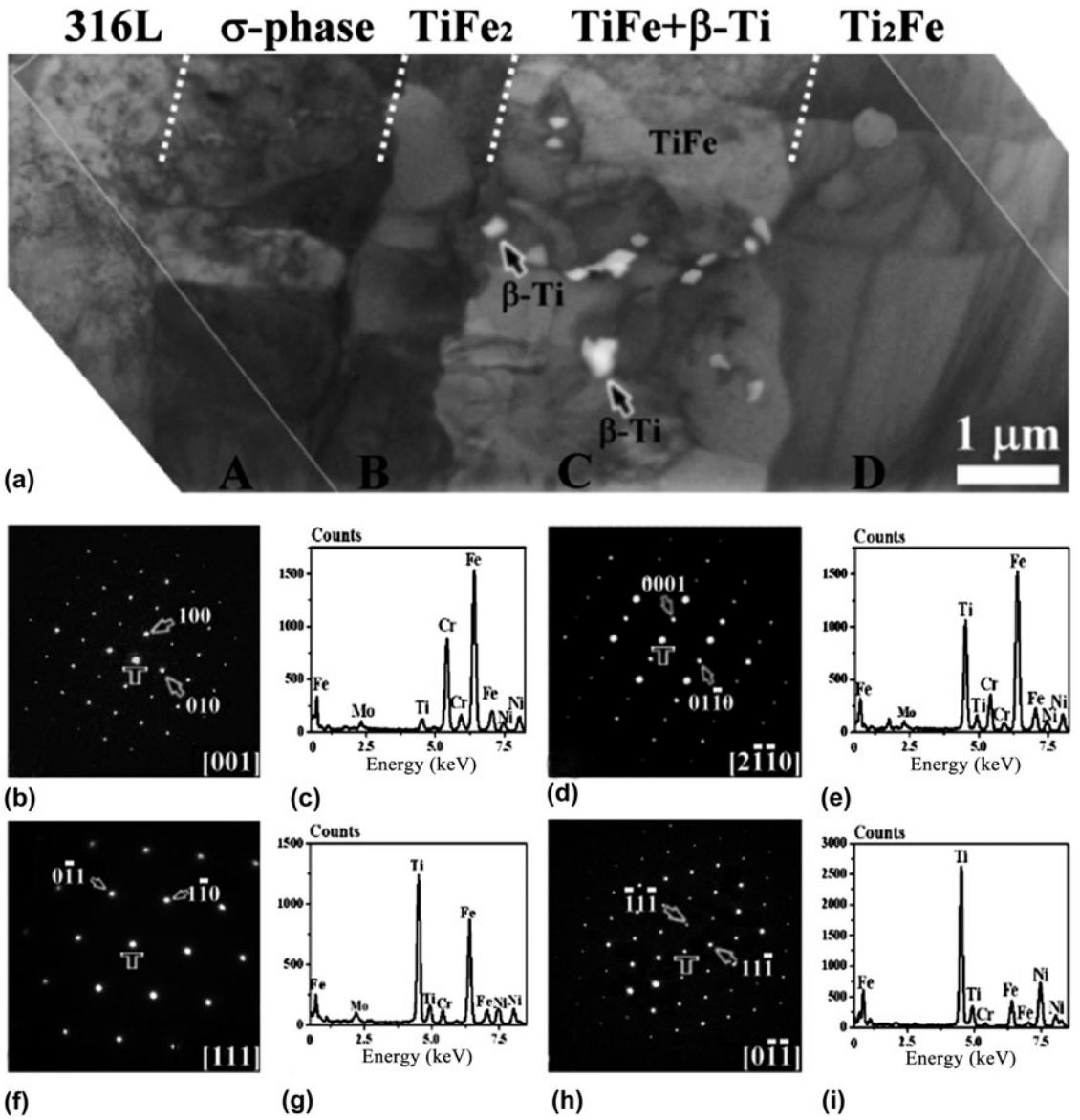

FIG. 3. TEM results of the microstructure: (a) morphology of zone I with σ-phase, $TiFe_2$, TiFe + β-Ti, and Ti_2Fe layers at the 316L/Ni interface; (b) SADP of the σ-phase with z = [001]; (c) EDS of the σ-phase; (d) SADP of $TiFe_2$ with z = $[2\bar{1}\bar{1}0]$; (e) EDS of $TiFe_2$; (f) SADP of the TiFe with z = [111]; (g) EDS of TiFe; (h) SADP of Ti_2Fe with z = $[0\bar{1}\bar{1}]$; (i) EDS of Ti_2Fe.

interdiffusion experiments involving titanium alloy and stainless steel, He et al.[28] reported that the formation of Ti_2Fe and TiFe occurred adjacent to the titanium alloys, whereas the $TiFe_2$ and the σ-phase occurred adjacent to the stainless steel.

B. Microstructure of the Ti/Ni interface

In Fig. 4(a), the BFI of a two-phase (Ti_2Ni + TiNi) region within layer F shows the granular morphology of Ti_2Ni, in between layers E and G, after annealing at 900 °C for 1 h. A lamellar morphology of Ti_2Ni + TiNi existed adjacent to the Ti_2Ni layer, as shown in Fig. 4(b). Figures 4(c) and 4(d) show the SADPs of the Ti_2Ni phase along the zone axes of [001] and $[\bar{1}12]$, respectively, corresponding to an fcc crystallographic structure with the calculated lattice parameter a = 1.19 nm (for comparison, Ti_2Ni: a = 1.131 nm in JCPDS #720442). From the EDS analyses shown in Fig. 4(e), the composition of the Ti_2Ni phase was 66.1 at.% Ti, 30.3 at.% Ni, and 3.6 at.% Cu (Ti:Ni = 66:30 ≈ 2:1). Figures 4(f) and 4(g) show the SADPs of the TiNi phase along the zone axes of [111] and [001], respectively, indicating that the phase had a simple cubic structure of the CsCl type with the calculated lattice parameter a = 0.32 nm (for comparison, TiNi: a = 0.2998 nm in JCPDS #180899). Figure 4(h) shows that the TiNi phase consisted of 45.4 at.% Ti, 48.9 at.% Ni, and 5.7 at.% Cu (Ti:Ni = 45:49 ≈ 1:1). Hinotani and Ohmori[19] reported that the structure of TiNi can be cubic

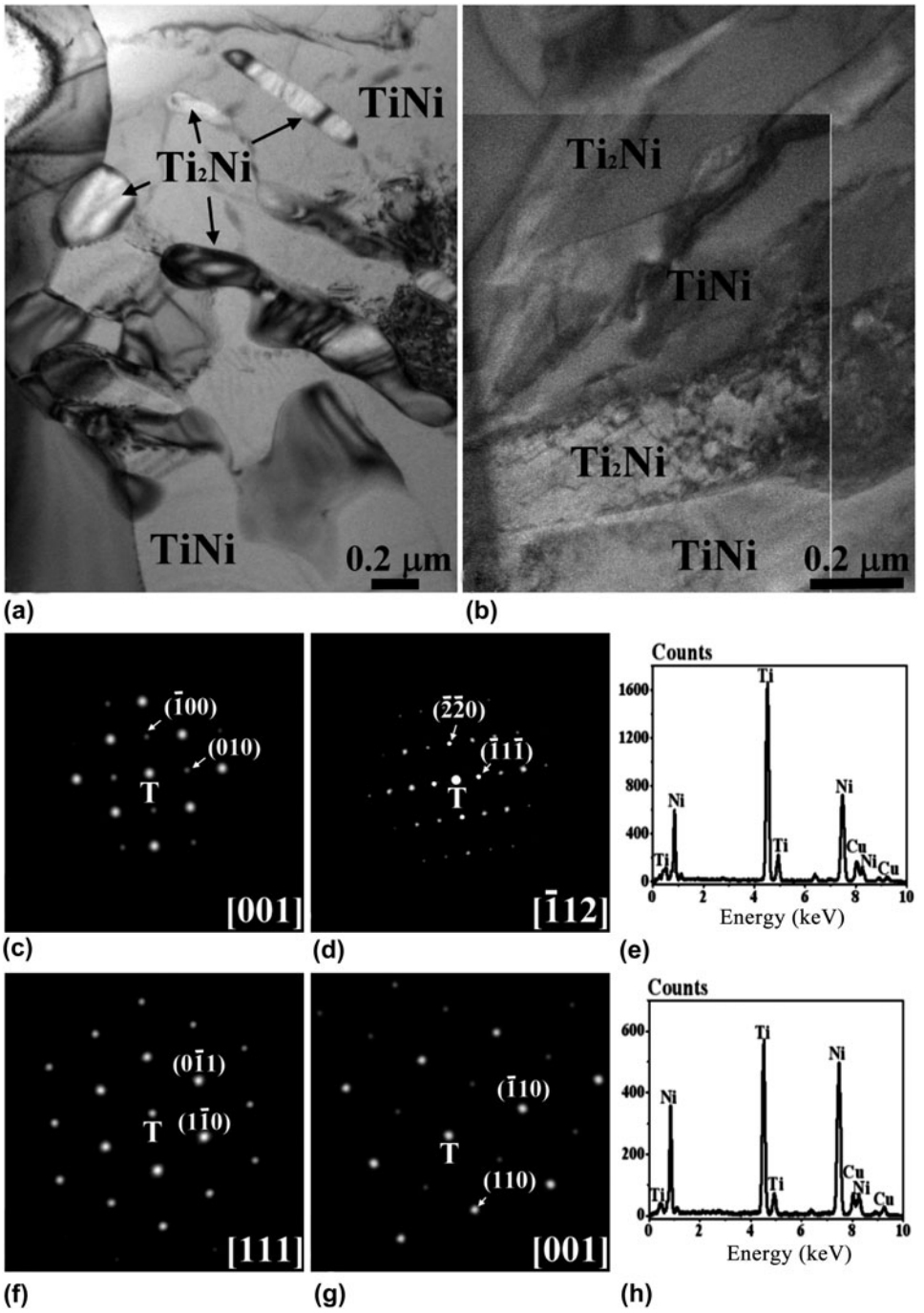

FIG. 4. TEM results of the microstructure: (a and b) morphology of zone II with the two-phase region of Ti_2Ni + TiNi after cooling from 900 °C; (c and d) SADPs of the Ti_2Ni phase with z = [001] and [1̄12], respectively; (e) EDS of the Ti_2Ni phase; (f and g) SADPs of the TiNi phase with z = [111] and [001], respectively; (h) EDS of the TiNi phase.

or monoclinic and is very sensitive to the compositions. A Ni concentration above 45 at.% results in a cubic TiNi phase, whereas a monoclinic TiNi phase forms below 45 at.% Ni. The granular Ti_2Ni, shown in Fig. 4(a), precipitated in the TiNi matrix during cooling, resulting in the formation of the Ni-enriched TiNi matrix. It was inferred that the precipitation of Ti_2Ni helped stabilize the cubic TiNi phase in reaction zone II.

C. Microstructure of the Ti/8Y-ZrO_2 interface

Figure 5(a) shows the BFI of reaction zone III with the TiO phase at the interface adjacent to the ZrO_{2-x} after annealing at 900 °C for 1 h. Figure 5(b) shows the SADP of TiO along the zone axis of [011], indicating that the TiO phase had the B1 (NaCl) structure and its lattice parameter was calculated as a = 0.43 nm (for comparison, TiO: a = 0.4185 nm in JCPDS

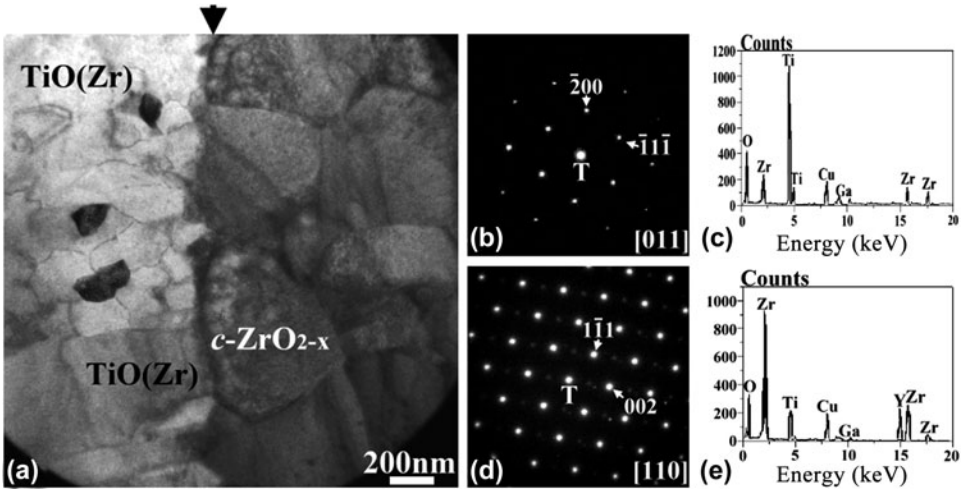

FIG. 5. TEM results of the microstructure: (a) morphology of the zone III with TiO and c-ZrO_{2-x} at the Ni/8Y-ZrO_2 interface; (b) SADP of the TiO with z = [011]; (c) EDS of TiO; (d) SADP of c-ZrO_{2-x} with z = [110]; (e) EDS of c-ZrO_{2-x}.

#772170). Figure 5(c) indicates that TiO was composed of 46.0 at.% Ti, 46.1 at.% O, 3.6 at.% Cu, 3.1 at.% Zr, and 1.2 at.% Ga. The peak of Ga was detected because of pollution by the focused ion beam. The c-ZrO_{2-x} was identified by the SADP acquired along the zone axis of [110] as shown in Fig. 5(d). Reflections of the type *odd*, *odd*, and *even* were not allowed for c-ZrO_{2-x}. However, the {112} type reflections appeared in the SADP of c-ZrO_{2-x} because a large concentration of oxygen vacancies changed its structure factor.[29] Figure 5(e) shows that the c-ZrO_{2-x} consisted of 56.7 at.% Zr, 31.7 at.% O, 4.6 at.% Ti, 2.4 at.% Cu, and 4.6 at.% Y. The yttrium (the stabilizer of ZrO_2) was insoluble in TiO (Fig. 5(c)) and retained in cubic zirconia [Fig. 5(e)]. Zirconia remained as a cubic phase because it dissolved Y_2O_3 as a stabilizer, leading to the formation of excess oxygen vacancies.[30,31] The TiO, Ti_3O, and Ti_6O layers formed at the joint interface between the (Cu-18Ga)-Ti melt and ZrO_2, whereas the TiO and Ti_2O reaction layers appeared at the YSZ/Ag-In-Ti alloy interface at temperatures ranging from 873 to 1150 K.[32,33] The existence of the TiO and ZrO_{2-x} indicated that redox occurred between Ti and ZrO_2.

D. Microstructure of residual Ti foils

Figure 6(a) displays a BFI of the needle-like α-Ti in the β-Ti matrix within the residual Ti foil between stainless steel 316L and Ni after annealing at 900 °C for 1 h. The β-Ti, which was stable at 900 °C, could be transformed into α-Ti during cooling. The needle-like α-Ti and the β-Ti were identified as hcp and bcc crystal structures, respectively, from the superimposed SADPs, as shown in Fig. 6(b). The orientation relationship between α-Ti and β-Ti were thus identified as follows: $[0001]_{\alpha-Ti}//[01\bar{1}]_{\beta-Ti}$ and $(02\bar{2}0)_{\alpha-Ti}//(211)_{\beta-Ti}$. At a higher magnification, Fig. 6(c) shows fine precipitates of the ω-phase in the β-Ti within the residual Ti between stainless steel 316L and Ni. Figure 6(d) shows the SADPs of the β + ω two-phase region. In addition to the strong bcc reflections of β-Ti, weak sharp spots corresponded to the two variants of the ω-phase (designated as ω_1 and ω_2). The SADPs were schematically redrawn in Fig. 6(e), with the diffraction spots being indexed, indicating that the orientation relations between the bcc β-Ti matrix and the hcp ω-phase were as follows: $[1\bar{1}0]_{\beta-Ti}//[1\bar{2}10]_{\omega}$ and $(111)_{\beta-Ti}//(0001)_{\omega}$. From the EDS analyses shown in Fig. 6(f), the β-Ti matrix contained 6.3 at.% β-Ti stabilizers (4.0 at.% Fe, 1.2 at.% Cr, and 1.1 at.% Ni) such that the β-Ti was retained at room temperature.[21] In contrast, the Fe, Cr, and Ni atoms were nearly insoluble in α-Ti. Furthermore, the retained β-Ti with Fe, Cr, and Ni in solid solution resulted in the phase transformation of β → β + ω during cooling, as detailed elsewhere.[34]

In brief, there were eight distinct reaction layers (A, B, C, etc.) in four distinct reaction zones (I, II, II, and III) of the stainless steel 316L/8Y-ZrO_2 joint with the Ti/Ni/Ti interlayer after annealing at 900 °C for 1 h. The compositions, the crystal structures, and the calculated lattice parameters corresponding to various layers are summarized in Table II. At the stainless steel 316L/Ti interface, Fe, Ni and Cr diffused from the stainless steel 316L into the Ti foil to a large extent, whereas a redox reaction occurred at the Ti/8Y-ZrO_2 interface. The interfacial reactions led to the formation of various Ti–Fe intermetallic layers and a TiO reaction layer, respectively. In Fig. 2, arrows indicate various original interfaces between different materials. In reaction zone I, it was believed that the original stainless steel 316L/Ti interface was located in the two-phase layer (TiFe + β-Ti, labeled as C) because Mo was nearly insoluble in the Ti foil. In reaction zone II, the original Ni/Ti interface was likely located at the interface of reaction layers F and G because the Kirkendall pores were observed in Ni. In reaction zone III, Y (the stabilizer of ZrO_2) was not detected in

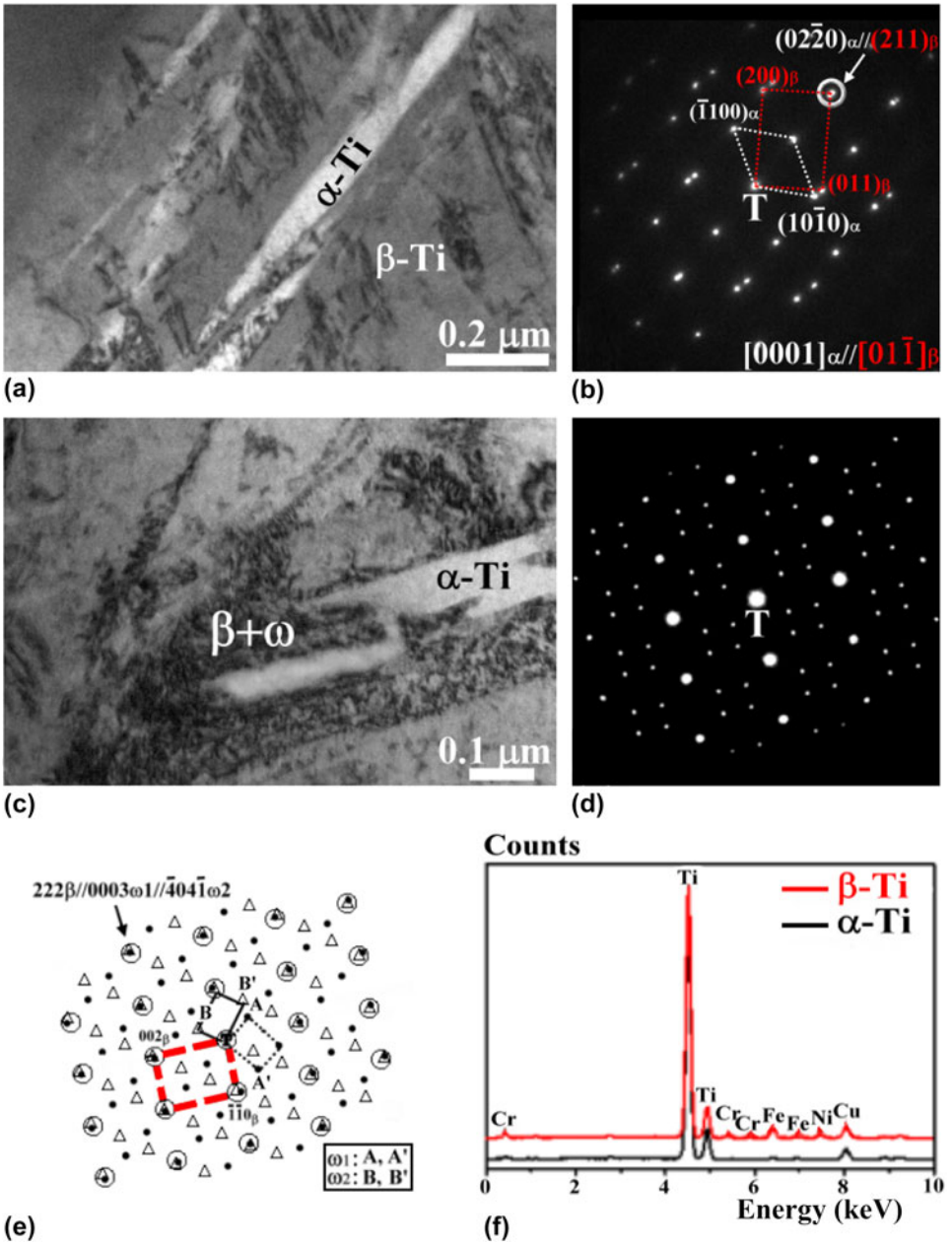

FIG. 6. TEM results of the residual Ti between 316L and Ni after annealing at 900 °C for 1 h: (a) morphology of the acicular α in the β-matrix; (b) SADPs of α-Ti and β-Ti, showing the orientation relationship of $[0001]_{\alpha-Ti}//[01\bar{1}]_{\beta-Ti}$ and $(02\bar{2}0)_{\alpha-Ti}//(211)_{\beta-Ti}$; (c) morphology of the ω precipitates in the β-Ti along with α-Ti; (d and e) SADPs of the β-Ti and ω phase and their schematic diagrams (O, β-Ti; ●, ω_1; Δ, ω_2) with zone axes of $[1\bar{1}0]_{\beta-Ti}//[1\bar{2}10]_{\omega}$ (A: $(10\bar{1}0)_{\omega1}$, A′: $(000\bar{1})_{\omega1}$; B: $(\bar{1}010)_{\omega2}$, B′: $(000\bar{1})_{\omega2}$); (f) EDS of α- and β-Ti in (a).

TiO, indicating the original Ti/8Y-ZrO_2 interface abutted a TiO layer (labeled H).

V. MICROSTRUCTURAL DEVELOPMENT AND PHASE FORMATION MECHANISM

The formation mechanism of individual reaction zones and residual Ti foils, as well as their microstructural development, at the interface of stainless steel 316L and 8Y-ZrO_2 are described below.

A. Reaction zone I

Figure 7(a) schematically presents the atomic movement of various species at the stainless steel 316L/Ti/Ni interfaces. Ti diffused into the stainless steel 316L and the Ni foil, whereas Fe, Ni, and Cr diffused into the Ti foil. Because the open structure of β-Ti formed at temperatures exceeding 882 °C, Fe, Ni and Cr atoms (from stainless steel 316L) and Ni atoms (from the Ni foil) traveled a longer distance in the Ti foil than Ti atoms did in the stainless steel 316L or the Ni foil. Figures 7(b) and 7(c)

TABLE II. Compositions[a] and crystal structures of phases formed at various zones after annealing at 900 °C for 1 h.

Reaction zone	Layer	Phase	Composition (at.%) Ti	Fe	Cr	Ni	Mo	Cu[b]	O	Zr	Ga[c]	Structures	Lattice parameter (nm)
Zone I	A	σ[d]	3.4	54.8	35.2	2.9	2.6	1.1	...	...	...	Tetragonal	$a = 0.91$, $c = 0.47$
	B	$TiFe_2$[e]	32.3	51.7	10.9	1.5	2.1	1.5	...	...	...	Hexagonal	$a = 0.50$, $c = 0.85$
	C	TiFe[e]	51.9	36.9	4.7	3.5	1.3	1.7	...	...	...	Simple cubic	$a = 0.30$
	C	β-Ti[d]	95.7	0.5	2.1	0.3	...	1.4	...	...	...	bcc	$a = 0.34$
	D	Ti_2Fe[e]	65.9	19.3	1.3	11.4	...	2.1	...	...	...	fcc	$a = 1.15$
Zone II	E	Ti_2Ni[e]	64.3	...	...	35.7	...	...	...	...	...	...	...
	F	TiNi[e]	45.4	...	...	48.9	...	5.7	...	...	...	Simple cubic	$a = 0.32$
	F	Ti_2Ni[d]	66.1	...	...	30.3	...	3.6	...	...	...	fcc	$a = 1.19$
	G	$TiNi_3$[e]	25.8	...	...	74.2	...	...	...	...	...	...	...
Zone III	H	TiO[e]	46.0	...	...	...	...	3.6	46.1	3.1	1.2	fcc	$a = 0.43$

[a]Ti_2Ni (E) and $TiNi_3$ (G) were analyzed using SEM/EDS, whereas other results were attained using TEM/EDS.
[b]Cu was caused by the pollution of the copper ring of TEM specimens.
[c]Ga was caused by the pollution of the focused ion beam during the preparation of TEM specimens.
[d]Formed during cooling.
[e]Formed during brazing.

illustrate the correlation between microstructural evolutions and the Fe–Ti binary phase diagram[35] at the stainless steel 316L/Ti interface on annealing. It was assumed that all the compositions at various cross sections along the longitudinal direction perpendicular to the interface could be determined by a horizontal solid-line (a tie line) at a specific temperature. The tie line crossed the fields of α-Fe, α-Fe + $TiFe_2$, $TiFe_2$, $TiFe_2$ + TiFe, TiFe, TiFe + Ti_2Fe, Ti_2Fe, Ti_2Fe + β-Ti, and β-Ti at 900 °C. These regions of α-Fe + $TiFe_2$, $TiFe_2$ + TiFe, TiFe + Ti_2Fe, and Ti_2Fe + β-Ti on the figure corresponded to the interfaces between α-Fe and $TiFe_2$, between $TiFe_2$ and TiFe, between TiFe and Ti_2Fe, and between Ti_2Fe and β-Ti, respectively (drawn by dashed lines). The binary phase diagram predicted the formation of the one-phase layer, whereas every two-phase region corresponded to the interface. As a result, the layers of α-Fe, $TiFe_2$, TiFe, Ti_2Fe, and β-Ti existed in sequence from stainless steel 316L to Ti in the stainless steel 316L/Ti/Ni joint at 900 °C, as shown in Fig. 7(c). The Ti_2Fe compound developed through a peritectoid reaction (TiFe + β-Ti → Ti_2Fe) near 1000 °C. Because the austenitic stainless steel 316L (γ-Fe) had 16–18 wt.% Cr, some residual ferrite (α-Fe) existed and facilitated the transformation to the σ-phase during cooling below 820 °C based on the Fr–Cr binary phase diagram.[36] Grot and Spruiell[37] mentioned that Ti and Mo in solid solutions favored the formation of the σ-phase because of the participation of these elements in the "equivalent Cr content" proposed by Hull.[38] Therefore, the σ-phase did not decompose into α-Fe and α-Cr. Moreover, a two-phase layer of TiFe + β-Ti formed at the $TiFe_2$/Ti_2Fe interface during cooling because the solubility of Ti in TiFe decreased with decreasing temperature. The precipitation of β-Ti can be expressed by the following reaction:

$$Ti_{1+x}Fe \rightarrow Ti_{1+y}Fe + (x-y)\beta - Ti \quad . \qquad (1)$$

The final microstructure of reaction zone I, formed after cooling from 900 °C, is displayed in Fig. 7(d).

B. Reaction zones II and III

Figure 7(e) schematically illustrates the diffusion of O and Ni atoms toward the Ti foil leading to the formation of various reaction layers at the Ni/Ti and Ti/8Y-ZrO_2 interfaces. The Ti–Ni phase diagram was used to explain the microstructure evolution at the Ni/Ti interface as shown in Fig. 7(f). The tie line (solid line) on the Ti–Ni phase diagram crossed the fields of Ni, Ni + $TiNi_3$, $TiNi_3$, $TiNi_3$ + TiNi, TiNi, TiNi + Ti_2Ni, Ti_2Ni, Ti_2Ni + β-Ti, and β-Ti at 900 °C. The interfaces of various reaction layers are represented by the regions Ni + $TiNi_3$, $TiNi_3$ + TiNi, TiNi + Ti_2Ni, and Ti_2Ni + β-Ti. As shown in Fig. 7(g), the reaction layers of $TiNi_3$, TiNi, Ti_2Ni, and β-Ti formed at the Ni/Ti interface adjacent to 8Y-ZrO_2 on annealing at 900 °C. Because of the Kirkendall effect, some pores appeared at the interface between Ni and $TiNi_3$.[19] Because the composition range of TiNi narrowed with decreasing temperature, the Ti_2Ni was precipitated so that the two-phase TiNi + Ti_2Ni layer (reaction layer F) was observed after cooling. According to the Ni–Ti phase diagram, the precipitation of Ti_2Ni or $TiNi_3$ can take place in the TiNi phase because of the decreasing solid solubility of Ni or Ti in the TiNi phase with decreasing temperature.[39] However, no $TiNi_3$ precipitates were found in the TiNi matrix because the cooling rate curve did not intersect with the TTT curve. A previous study indicated that $TiNi_3$ occurs as the equilibrium phase at higher aging temperatures and longer aging

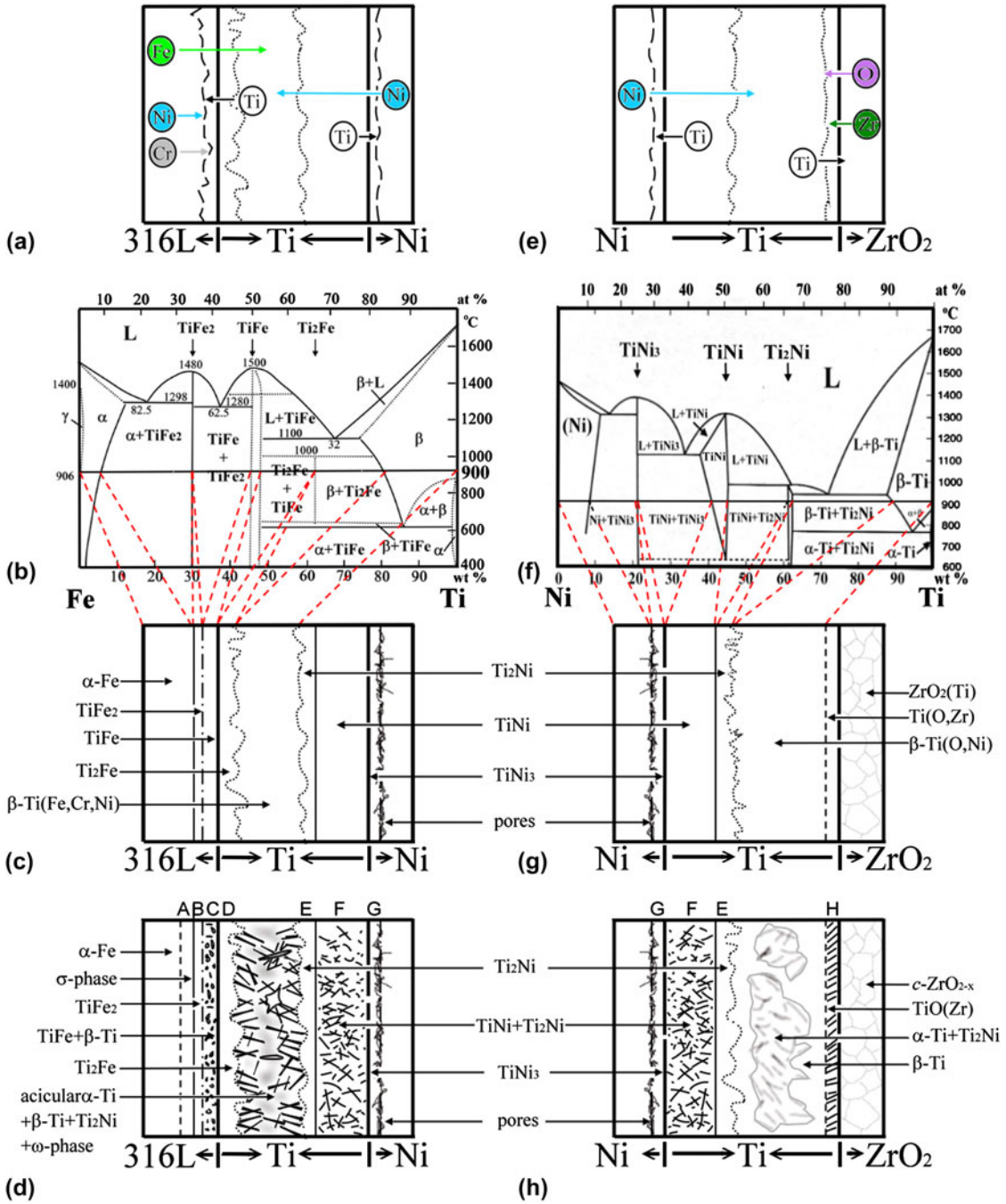

FIG. 7. Microstructural evolution of the 316L/Ti/Ni/Ti/8Y-ZrO_2 joint after annealing at 900 °C for 1 h. (a) An illustration of atomic diffusions at the 316L/Ni interfaces; (b) a tie line drawn in the Ti–Fe phase diagram at 900 °C; (c) the microstructures of 316L/Ti/Ni joint at 900 °C; (d) the 316L/Ti/Ni joint after cooling; (e) an illustration of atomic diffusions at Ni/8Y-ZrO_2 interfaces; (f) a tie line drawn in the Ti–Ni phase diagram at 900 °C; (g) the microstructures of Ni/Ti/8Y-ZrO_2 joint at 900 °C, and (h) the Ni/Ti/8Y-ZrO_2 joint after cooling.

time.[40] On annealing at 900 °C, the Ni atoms of TiNi (layer F) diffused outwards into the residual Ti, leading to the growth of reaction layer Ti_2Ni (layer E). Reaction layer F thus had a columnar TiNi structure, parallel to the direction of Ni diffusion, in reaction zone II. The formation of the columnar TiNi is expressed as follows:

$$3\mathrm{TiNi}_{(\text{homogeneous})} \rightarrow \mathrm{TiNi}_{(\text{columnar})} + \mathrm{Ti_2Ni}_{(\text{columnar})} + \mathrm{Ni}_{(\text{diffused into layer E})} \quad . \qquad (2)$$

Furthermore, on annealing at 900 °C, the oxidation and reduction reactions led to the formation of TiO and ZrO_{2-x}, respectively. Because Ti had an affinity for O, the

reduction of ZrO_2 led to the formation of the TiO layer as well as oxygen-deficient zirconia (ZrO_{2-x}), even though the Ellingham diagram indicated that ZrO_2 was more thermodynamically stable than TiO_2. It was inferred that ZrO_2 was not completely reduced to the metallic Zr, and Ti was not oxidized to TiO_2, in the partial reduction process mentioned above. Chang et al. reported that the existence of the TiO reaction layer in the diffusion couples of Ti and CaO/ZrO_2 composites after reaction at 1550 °C for 6 h dramatically inhibited the diffusion of Zr out of ZrO_{2-x}.[20] The final microstructure of reaction zones II and III after cooling from 900 °C is schematically shown in Fig. 7(h).

C. Two residual Ti foils

On annealing at 900 °C, Fe, Cr, and Ni diffused into the residual Ti foil, which was located between zones I and II. Because Fe, Cr, and Ni were stabilizers for β-Ti, β-Ti was the major phase, as expected. β-Ti was partially transformed into acicular α-Ti on cooling, and the ω-phase precipitated from the retained β-Ti at lower temperatures, based on the following reactions:

$$\beta\text{-Ti} \rightarrow \text{retained } \beta\text{-Ti} + \alpha\text{-Ti } (882^{\circ}\text{C}) \quad , \qquad (3)$$

$$\beta\text{-Ti} \rightarrow \beta\text{-Ti} + \omega\text{-phase } (450^{\circ}\text{C}) \quad . \qquad (4)$$

In addition, the Ti_2Ni islands were surrounded by acicular α-Ti in the β-Ti matrix because most of the Ni atoms diffused out of β-Ti grains. For comparison, the β-phase was completely retained in alloys with the critical solute concentrations such as Ti–Ni (7–7.5 at.%), Ti–Fe (7 at.%), and Ti–Cr (12 at.%).[41] The precipitation of the ω-phase in the residual Ti between the stainless steel 316L and Ni could be attributed to the following factors. First, the diffusion of Fe, Cr, and Ni into the residual Ti foil on annealing made the ω-phase formation thermodynamically favorable. Second, the slow cooling rate (3°C/min) created a favorable kinetic condition for ω-phase formation. Moffat and Larbalestier reported that a higher cooling rate favored the formation of α martensite, but a slower cooling rate favored the formation of the ω-phase in Ti–Nb alloys.[42] In this study, approximately 5.7 at.% of Fe, Cr, and Ni was dissolved in β-Ti at high temperatures, resulting in the direct transformation of β → β + ω during cooling. The final microstructure of the residual Ti foil between zones I and II after cooling is schematically represented in Fig. 7(g).

The phase transformation of the residual Ti foil between reaction zones II and III is described as follows. The residual Ti foil transformed into the β-phase on annealing at 900 °C with the diffusing O and Ni atoms as solid solutions. The β-phase partially decomposed into a eutectoid structure of α-Ti + Ti_2Ni during the subsequent cooling. Based on the Ni–Ti phase diagram, a hypereutectoid reaction is expressed by the following two steps:

$$\beta\text{-Ti} \rightarrow \beta\text{-Ti} + p\text{-}Ti_2Ni \text{ (proeutectoid } Ti_2Ni) \quad , \qquad (5)$$

$$\beta\text{-Ti} \rightarrow \alpha\text{-Ti} + e\text{-}Ti_2Ni \text{ (eutectoid } Ti_2Ni) \quad . \qquad (6)$$

No ω-phase was found in the residual Ti between Ni and 8Y-ZrO_2 because of two factors: (1) Sufficient β-stabilizer (Ni ~ 10.9 at.%) completely stabilized β-Ti[41] and (2) the O addition reduced the volume fraction, the upper temperature limit of formation, and the stability time of the ω-phase.[43] This result is consistent with the absence of a transitional ω-phase detected in the Ti–Ni alloy.[44] The final microstructure of the residual Ti foil between zones II and III after cooling is schematically shown in Fig. 7(h). The two foils had distinct differences in microstructures.

VI. SUMMARY AND CONCLUSIONS

A Ti/Ni/Ti multilayer was successfully used to bond a stainless steel 316L/8Y-ZrO_2 joint after annealing at 900 °C for 1 h in Ar. The microstructures of the various interfaces and the residual Ti were characterized using analytical electron microscopy. Four distinct layers of σ-phase, $TiFe_2$, TiFe + β-Ti, and Ti_2Fe were observed at the stainless steel 316L/Ti interface, and three reaction layers of Ti_2Ni, TiNi + Ti_2Ni, and $TiNi_3$ were observed at the Ti/Ni interface during cooling. The high chemical affinity of Ti for O led to the formation of TiO as well as c-ZrO_{2-x} at the Ti/8Y-ZrO_2 interface. A two-phase structure of ω-phase and β-Ti as well as acicular α-Ti was found in the residual Ti between the stainless steel 316L and Ni, where the metastable retained β-Ti contained approximately 5.7 at.% β-stabilizers (Fe, Cr, and Ni). The ω-phase formation mechanism was the outward diffusion of Fe and Cr from the stainless steel into the Ti foil. The ω precipitates nucleated and grew in the β-matrix with the following two variants: $\langle 1\bar{1}0\rangle_{\beta\text{-Ti}}//\langle 1\bar{2}10\rangle_{\omega}$ and $\{111\}_{\beta\text{-Ti}}//\{0001\}_{\omega}$. However, no ω precipitate was observed in the other residual Ti between Ni and 8Y-ZrO_2, where β-Ti (Ni, O) was retained with some exceptions. A lamellar eutectoid structure (α-Ti and e-Ti_2Ni) was also found in the retained β-Ti.

ACKNOWLEDGMENT

This research was supported by the National Science Council (Taiwan) under Contract No. NSC98-2221-E-009-039-MY2.

REFERENCES

1. N.Q. Minh: Ceramic fuel cells. *J. Am. Ceram. Soc.* **76**(3), 563 (1993).

2. C.H. Cheng, Y.W. Chang, and C.W. Hong: Multiscale parametric studies on the transport phenomenon of a solid oxide fuel cell. *J. Fuel Cell Sci. Technol.* **2**(4), 219 (2005).
3. R.M. Ormerod: Solid oxide fuel cells. *Chem. Soc. Rev.* **32**(1), 17 (2003).
4. W.Z. Zhu and S.C. Deevi: Development of interconnect materials for solid oxide fuel cells. *Mater. Sci. Eng. A* **348**(1–2), 227 (2003).
5. I. Antepara, I. Villarreal, L.M. Rodríguez-Martínez, N. Lecanda, U. Castro, and A. Laresgoiti: Evaluation of ferritic steels for use as interconnects and porous metal supports in IT-SOFCs. *J. Power Sources* **151**, 103 (2005).
6. M. Singh, T.P. Shpargel, and R. Asthana: Brazing of stainless steel to yttria-stabilized zirconia using gold-based brazes for solid oxide fuel cell applications. *Int. J. Appl. Ceram. Technol.* **4**(2), 119 (2007).
7. S. Molin, M. Gazda, B. Kusz, and P. Jasinski: Evolution of 316L porous stainless steel for SOFC support. *J. Eur. Ceram. Soc.* **29**, 757 (2009).
8. L. Niewolak, E. Wessel, L. Singheiser, and W.J. Quadakkers: Potential suitability of ferritic and austenitic steels as interconnect materials for solid oxide fuel cells operating at 600°C. *J. Power Sources* **195**, 7600 (2010).
9. F. Smeacetto, M. Salvo, M. Ferraris, V. Casalegno, and P. Asinari: Glass and composite seals for the joining of YSZ to metallic interconnect in solid oxide fuel cells. *J. Eur. Ceram. Soc.* **28**(3), 611 (2008).
10. G.W. Liu, W. Li, G.J. Qiao, H.J. Wang, J.F. Yang, and T.J. Lu: Microstructures and interfacial behavior of zirconia/stainless steel joint prepared by pressureless active brazing. *J. Alloys Compd.* **470**(1–2), 163 (2009).
11. M. Singh, T.P. Shpargel, and R. Asthana: Braze oxidation behavior and joint microstructure in YSZ/steel joints made using palladium brazes for SOFC applications. *Mater. Sci. Eng. A* **485**(1–2), 695 (2008).
12. C. Zheng, H. Lou, Z. Fei, and Z. Li: Partial transient liquid-phase bonding of Si_3N_4 with Ti/Cu/Ni multi-interlayers. *J. Mat. Sci. Lett.* **16**(24), 2026 (1997).
13. M. Paulasto, G. Ceccone, and S.D. Peteves: Joining of silicon nitride via a transient liquid. *Scr. Mater.* **36**(10), 1167 (1997).
14. R. Chen, D. Zuo, and M. Wang: Improvement of joint strength of SiCp/A1 metal matrix composite in transient liquid phase bonding using Cu/Ni/Cu film interlayer. *J. Mater. Sci. Technol.* **22**(3), 291 (2006).
15. G.J. Qiao, H.J. Wang, J.Q. Gao, and Z.H. Jin: Brazing Al_2O_3 to Kovar alloy with Ni/Ti/Ni interlayer and dramatic increasing of joint strength after thermal cycles. *Mater. Sci. Forum* **486–487**, 481 (2005).
16. O. Smorygo, J.S. Kim, M.D. Kim, and T.G. Eom: Evolution of the interlayer microstructure and the fracture modes of the zirconia/Cu-Ag-Ti filler/Ti active brazing joints. *Mater. Lett.* **61**(2), 613 (2007).
17. Z.G. Wang, N. Kato, K. Sasaki, T. Hirayama, and H. Saka: Electron holographic mapping of two-dimensional doping areas in cross-sectional device specimens prepared by the lift-out technique based on a focused ion beam. *J. Electron Microsc.* **53**(2), 115 (2004).
18. G. Cliff and G.W. Lorimer: The quantitative analysis of thin specimens. *J. Microsc.* **103**(2), 203 (1975).
19. S. Hinotani and Y. Ohmori: The microstructure of diffusion-bonded Ti/Ni interface. *Trans. Jpn. Inst. Met.* **29**, 116 (1988).
20. Y.W. Chang and C.C. Lin: Compositional dependence of phase formation mechanisms at the interface between titanium and calcia-stabilized zirconia at 1550°C. *J. Am. Ceram. Soc.* **93**(11), 3893 (2010).
21. M. Ghosh, K. Bhanumurthy, G.B. Kale, J. Krishnan, and S. Chatterjee: Diffusion bonding of titanium to 304 stainless steel. *J. Nucl. Mater.* **322**(2–3), 235 (2003).
22. M. Ghosh and S. Chatterjee: Diffusion bonded transition joints of titanium to stainless steel with improved properties. *Mater. Sci. Eng. A* **358**(1–2), 152 (2003).
23. M. Ghosha, S. Chatterjee, and B. Mishra: The effect of intermetallics on the strength properties of diffusion bonds formed between Ti-5.5Al-2.4V and 304 stainless steel. *Mater. Sci. Eng. A* **363**(1–2), 268 (2003).
24. N. Orhan, T.I. Khan, and M. Eroglu: Diffusion bonding of a microduplex stainless steel to Ti-6Al-4V. *Scr. Mater.* **45**(4), 441 (2001).
25. K.A. Gschneidner, Jr. and M. Verkade: Electronic and crystal structures, size (ECS^2) model for predicting binary solid solutions. *Prog. Mater. Sci.* **49**(3–4), 411 (2004).
26. H. Qin, J. Hu, B. Li, M. Zhao, X. Liu, and J. Chen: $Fe_{74.5-x}Cu_xV_3Si_{13.5}B_9$ as-spun ribbons prepared by melt-spinning technique. *Mater. Trans.* **49**, 2761 (2008).
27. J.L. Murray: The Fe-Ti (iron-titanium) system. *Bull. Alloy Phase Diagrams* **2**(3), 320 (1981).
28. P. He, J.H. Zhang, and X.Q. Li: Diffusion bonding of titanium alloy to stainless steel wire mesh. *Mater. Sci. Technol.* **17**, 1158 (2001).
29. K.L. Lin and C.C. Lin: Reaction between titanium and zirconia powders during sintering at 1500°C. *J. Am. Ceram. Soc.* **90**(7), 2220 (2007).
30. K.L. Lin and C.C. Lin: Effects of annealing temperature on microstructural development at the interface between zirconia and titanium. *J. Am. Ceram. Soc.* **90**(3), 893 (2007).
31. C.C. Lin, Y.W. Chang, K.L. Lin, and K.F. Lin: Effect of yttria on interfacial reactions between titanium melt and hot-pressed yttria/zirconia composites at 1700°C. *J. Am. Ceram. Soc.* **91**(7), 2321 (2008).
32. V.M. Perevertailo, O.B. Loginova, and N.G. Bagno: Interaction between metal melts and zirconium dioxide. *Trans. JWRI* **30**, 143 (2001).
33. X.M. Xue, J.T. Wang, and Z.T. Sui: Wettability and interfacial reaction of alumina and zirconia by reactive silver-indium base alloy at mid-temperatures. *J. Mater. Sci.* **28**(5), 1317 (1993).
34. B.S. Hickman: The formation of omega phase in titanium and zirconium alloys: A review. *J. Mater. Sci.* **4**(6), 554 (1969).
35. I.I. Kornilov and N.G. Boriskina: The Ti-Fe phase diagram. *Dokl. Akad. Nauk SSSR* **108**, 1083 (1956).
36. V.P. Itkin: Cr-Fe (Chromium-Iron), in *Phase Diagrams of Binary Iron Alloys*, H. Okamoto ed.; ASM International, Metal Park, OH, 1993, p. 102.
37. A.S. Grot and J.E. Spruiell: Microstructural stability of titanium-modified type 316 and type 321 stainless steel. *Metall. Mater. Trans. A* **6**(11), 2023 (1975).
38. F.C. Hull: Effects of composition on embrittlement of austenitic stainless steel. *Weld. Res. Suppl.* **52**, S104 (1973).
39. G.F. Bastin and G.D. Rieck: Diffusion in the titanium-nickel system: I. occurrence and growth of the various intermetallic compounds. *Metall. Mater. Trans. B* **5**(8), 1817 (1974).
40. M. Nishida, C.M. Wayman, and T. Honma: Precipitation processes in near-equiatomic TiNi shape memory alloys. *Metall. Mater. Trans. A* **17**(9), 1505 (1986).
41. E.W. Hare and D.H. Polonis: Electrical resistivity-constitution relationships in Ti-Fe and Ti-Ni alloys. *J. Mater. Sci.: Mater. Electron.* **1**(1), 25 (1990).
42. D.L. Moffat and D.C. Larbalestier: The competition between martensite and omega in quenched Ti-Nb alloys. *Metall. Trans. A* **19**(7), 1677 (1988).
43. J.C. Williams, B.S. Hickamn, and D.H. Leslie: The effect of ternary additions on the decomposition of metastable beta-phase titanium alloys. *Metall. Trans.* **2**(2), 477 (1971).
44. D.H. Polonis: Phase Transformations in Titanium-Rich Alloys with Iron and Nickel. Ph.D. Thesis, University of British Columbia, BC, Canada, 1955, pp. 65.